Claudia Redenbach[a], Alexander Rack[b], Katja Schladitz[c], Oliver Wirjadi[c], Michael Godehardt[c]

[a]University of Kaiserslautern, Mathematics Department, Kaiserslautern, Germany
[b]European Synchrotron Radiation Facility, Grenoble, France
[c]Fraunhofer ITWM, Department Image Processing, Kaiserslautern, Germany

Beyond imaging: on the quantitative analysis of tomographic volume data

Tomographic techniques are a valuable analytical tool as they deliver spatial information of a specimen in a truly three-dimensional manner. Both computed tomography with high spatial resolution and quantitative volume image analysis have made enormous progress during the last decade. In particular in materials and natural science applications the combination of high-resolution three-dimensional imaging and the subsequent image analysis exploiting the fully preserved spatial structural information yield new and exciting insight.

In this paper, field-tested and up-to-date methods for tomographic imaging of microstructures, for processing and for quantitatively analysing three-dimensional images are introduced. By selected applications from materials research, this article shall underline the importance of volume image analysis as a crucial step in order to go beyond the images: it allows for determining spatial cross-correlations between different constituents of a specimen, to investigate orientations or to derive statistically relevant information like size distributions. The core part of the paper consists, besides the exemplary application scenarios, in the processing chain, the tools and methods used.

1 Introduction

Microtomography yields attractive and impressive images of, e. g., microstructures of foams, fiber composites, snow, lichen or soil. This is particularly important for weak or highly porous materials whose microstructures could not be imaged by classical techniques like materialography involving serial slicing and microscopic imaging. The use of microtomography enables three-dimensional (3D) visualisation and virtual slicing of the sample and thus boosts understanding. Quantitative image analysis goes one step further beyond plain imaging: yielding a quantitative description of the microstructure. Exploiting the full spatial information contained in 3D images allows, e. g., for detailed directional analyses, estimation of particle size distributions without shape assumptions, or judging the 3D connectivity of a structure, just to name a few. Moreover, macroscopic materials properties like mechanical strength, permeability, or acoustic absorption can be simulated in the 3D images or in geometric models fit to the microstructure. Many image processing and analysis algorithms are algorithmically and computationally one magnitude more complex in 3D than in 2D. Furthermore, basic image processing concepts like neighborhoods have to be rethought when moving on to the third dimension.

The outline of this paper is arranged around an overview on tomographic techniques, followed by a discussion of basic image processing techniques such as filtering or segmentation which play an important role in the preparation of images for quantitative analysis. Then, use cases of quantitative image analysis are presented, introducing appropriate methods for different kinds of materials.

2 Tomographic Imaging

Initially, the acronym tomography (from the Greek words $\tau \acute{o} \mu o \varsigma$ [tomos] in the sense of *to cut* and $\gamma \rho \acute{a} \varphi \varepsilon \iota \nu$ [graphein] for *to draw*) was solely associated with the so-called computed-axial scanning tomography (CAT) scanners for which G. N. Houndsfield and A. M. Cormack were presented the Nobel Prize for Physiology or Medicine in 1979. The basic idea of computed tomography is that the inner mass distribution of a specimen can be virtually reconstructed using projection images taken under different angles of view. Nowadays, tomographic techniques are considered in a broader manner as any imaging method which delivers cross-sectional pictures of the specimen under study. Besides non-destructive techniques based on, e. g., penetrating radiation, also destructive techniques like the three-dimensional atom probe, cf. [5] or a milling focused ion-beam, cf. [28] are considered frequently as tomographic methods.

Within the framework of this article, a brief introduction to computed tomography (CT) using penetrating radiation shall be given. More precisely, ionizing radiation is used, i. e. hard X-rays from laboratory or synchrotron-based sources. Furthermore, as high spatial resolutions are employed, frequently one uses the term microtomography (µCT), cf. [43]. Further details, especially considering the use of alternative types of radiation like neutrons or electrons are published elsewhere, cf. [3]. Likewise, specific techniques like positron-emission tomography which are mainly applied in medicine are not within the scope of this article, cf. [21].

For a standard µCT scan, the sample is placed on a rotation stage with the detector being at a fixed position (contrary to medical CT, where the detector is moved and the patient remains at a fixed position). The sample is illuminated while rotating, the transmitted radiation is recorded downstream of the sample. Nowadays, area detectors are employed to record two-dimensional radiographic images of the sample: µCT is also frequently called a full-field method, contrary to scanning techniques introduced later in this paragraph. When neglecting scattering and diffraction effects, the recorded images represent the attenuation of the sample. More precisely, each image element (pixel) is associated with a line integral of the X-ray attenuation along the corresponding X-ray beam path. Different approaches exist to virtually reconstruct the inner mass distribution of the sample from the projection images taken at different angles of view (see, e. g., [23]): the problem can be formulated as set of independent equations, to be solved (in an iterative manner) by algebraic methods. Alternatively, a summation of the measured integral attenuation profiles in real or Fourier space can be performed (filtered-backprojection algorithm or the direct Fourier inversion). The reconstruction is performed cross-sectional slice by cross-sectional slice yielding a complete tomographic volume image consisting of a stack of cross-sectional slices.

The early developments of hard X-ray µCT until the end of the last millennium were dominated by the quest for the ultimate resolution. The technical developments established X-ray µCT as unique analytical tool, with high spatial resolutions achievable by using either laboratory or synchrotron-based sources, cf., e. g. [12]. The more recent developments are focusing on novel contrast schemes with either increased sensitivity or complementary contrast modes on one side, and on high data acquisition speed towards real-time three-dimensional tomographic imaging on the other.

The advantage of employing laboratory X-ray sources for µCT clearly is the easy access together with the drastically reduced costs compared to large-scale facilities. Synchrotron light sources remain the first choice for flagship applications being either novel techniques, delicate samples or both. Using the intense flux of synchrotron light sources allowed already for increasing the contrast, more exactly the sensitivity by introducing sophisticated methods like holotomography (see [9]), analyzer-based imaging (cf., e. g. [8]) or grating-based interferometry (cf., e. g. [48]). Briefly, these methods, frequently called phase-sensitive imaging, measure directly or indirectly the local electron density rather than the local mass density like in absorption-based X-ray imaging. The latter, being also very depending on the available photon flux density, benefits from the use of synchrotron light sources as well: the number of photons emitted allows to push the density-related material contrast [7]. In the case where polychromatic radiation is employed rather than (quasi-)monochromatic, a further gain of photon flux density is reached. Subsequently, data acquisition speed can be increased dramatically, allowing to acquire, e. g., several 10 000 X-ray images per second. This allows to follow fast processes in two dimensions with a time-resolution down to the microsecond range or to perform tomographic scans in the range of seconds [37]. Contrary, monochromatic radiation and the common high photon flux density is required when µCT is combined with classical diffraction imaging on crystals (X-ray topography) to track grains in three dimensions (see, e. g. [24]). Independently of the flux, different tomographic geometries are available to access three-dimensional images of flat objects, which generally can be considered as a challenge for classical µCT due to their shape (cf., e. g. [16] and [18]).

In the last years, scanning tomographic techniques are employed more frequently, as they allow for contrast modes completely complementary to the ones listed above. Scanning a sample through the focal spot of an X-ray optical system allows for example to collect the fluorescence signal and/or the powder-diffraction signal which gives, via confocal approaches or by tomographic techniques, access to the local chemical species distribution, local strain or the distribution of crystalline phases within the probed sample (cf., e. g. [6, 26, 44, 52]). The imaging sensitivity is further increased when Ptychographic tomography is employed, which also increases the demands on the coherence of the source (see [11]).

Within this article, the aim is to show how to go beyond imaging, i. e. to use the highly resolved, rich-contrasted images as the basis for a quantitative image analysis. A step, which is of crucial importance as most applications, e. g. from materials research, do not only require an image but a sound quantitative analysis. As an example, a microtomographic dataset of two joint glass-fibre reinforced polymer plates is shown in Fig. 1: the glass fibres are visible in an excellent manner, thanks to the high contrast (data was taken at the BAM*line* of the BESSY-II light source, Germany, see [39]). A common question which cannot be answered by a plain volume rendering is, if the orientation of the fibres changes with respect to their distance to the place where the plates are joined [50].

3   Image processing

The topic of image processing covers the gap between image acquisition and image analysis, i.e., its purpose is to prepare the raw image data for subsequent measurements. From the wide range of methods for image denoising and smoothing, contrast enhancement, grey value equalisation, or edge detection, only a very narrow choice motivated by the use cases presented in Section 4 is explained here.

In general one has to keep in mind that in 3D some sophisticated methods developed for 2D images are not applicable due to their forbidding computation time or memory requirements. Moreover, aiming at a quantitative analysis at the end, everything that would bias the analysis has to be avoided.

In most cases, the final processing step is segmentation, which – in general – describes the process of separating an image into disjoint areas which contain the objects or phases of interest – depending on the
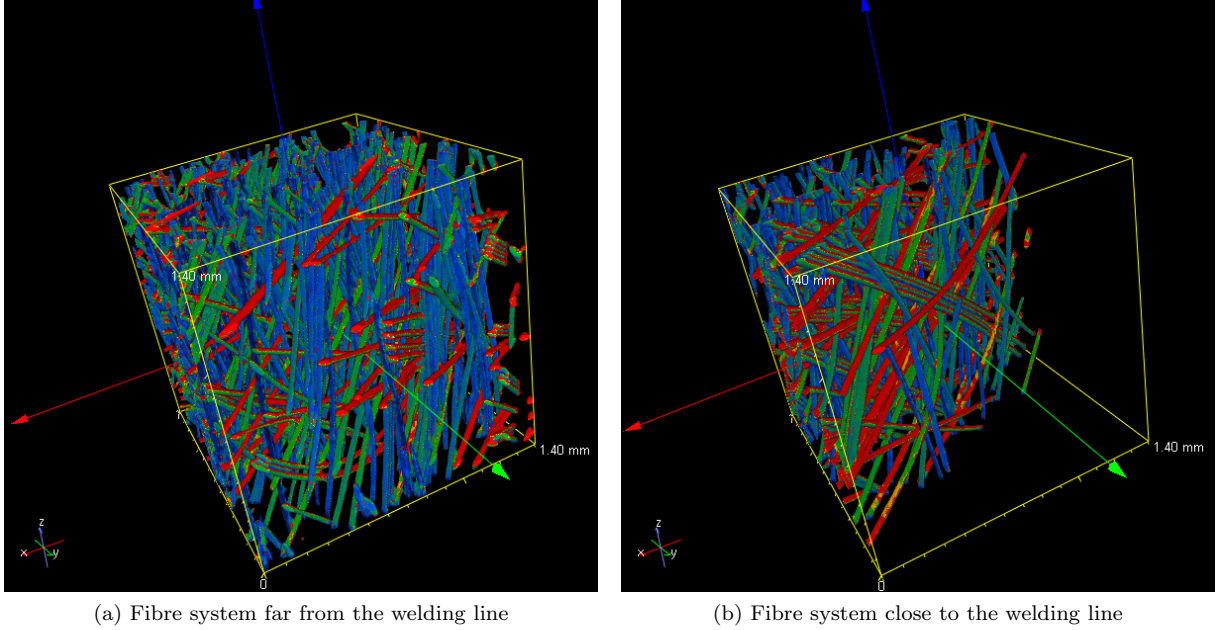
(a) Fibre system far from the welding line   (b) Fibre system close to the welding line

Figure 1: Subvolumes of a glass fibre reinforced polymer with a welded join and estimated local fibre directions. Sample: Institut für Verbundwerkstoffe Kaiserslautern. Imaging: A. Rack, ESRF, phase contrast mode. Pixel size $3.5\,\mu$m, total sample size approximately $7 \times 7 \times 3\,\text{mm}^3$, analysed subvolumes $(1.4\,\text{mm})^3$, [50]. The colours code the θ component of the local fibre directions in polar coordinates with blue corresponding to the z-axis ($\theta = 0$) and red to $\theta = \pi/2$.

context. For most image analysis tasks, image segmentation is a prerequisite, as it allows for measuring size, shape, orientation and other properties from an image.

3.1   Images and adjacency systems

Let $\mathbb{L} = (s_1, s_2, s_3)\mathbb{Z}^3$ be a three-dimensional cuboidal lattice with lattice spacings $s_1, s_2, s_3 > 0$. For all image data used in this paper we have $s_1 = s_2 = s_3 = s$, the analysis methods work nevertheless in the general setting, too. Denote by $W \subset \mathbb{R}^3$ a cuboidal observation window. An image in our sense is a function

$$f : \mathbb{L} \cap W \longrightarrow V$$

where V is the set of real or complex numbers $\mathbb{R}$, $\mathbb{C}$, or $V = \{0, \ldots, 2^n - 1\}$ with $n = 1, 8, 16$ or 32. If $V = \{0, 1\}$ then f is called binary image. In this case the image is often described as a set $X \subset \mathbb{R}^3$ observed at the lattice points within the observation window, that is the intersection $X \cap \mathbb{L} \cap W$. The function f is then just the indicator function of X, restricted to the observable points $f = \mathbb{I}_X|_{\mathbb{L} \cap W}$, hence $f(x) = 1$ if $x \in X\mathbb{L} \cap W$ and $f(x) = 0$ otherwise. The term pixel or voxel is used for both $x \in \mathbb{L} \cap W$ as well as the pair $(x, f(x))$. In a slight abuse of notation we speak of the lattice spacing s as pixel size, too. For processing as well as analysis, the discrete connectivity within the image is crucial. In 2D, the neighbourhood of a pixel x is completely described by the edges connecting x to its direct neighbours. In 3D, an unambiguous description needs to be more detailed. We therefore use adjacency systems consisting of vertices, edges, faces, and cells, instead of neighbourhoods following [31]. Let $C = [0, s]^3$ be the unit cell of the lattice $\mathbb{L}$. Its vertices can be written as $a(v_1, v_2, v_3)$ with $v_i \in \{0, 1\}$, $i = 1, 2, 3$ and binarily coded by $2^{v_1 + 2v_2 + 4v_3}$.

The 256 subsets ξ_ℓ, $\ell = 0, \ldots, 255$, of vertices of C can then uniquely be indexed by the sum of the codes of their elements. A local adjacency system is formed by convex hulls $F_\ell = \text{conv}\xi_\ell$ of subsets of vertices of C fulfilling a number of consistency conditions [33, Definition 3.2]. Translation of the local

adjacency system into all lattice points then yields the adjacency system. The maximal adjacency system $\mathbb{F}_{26} = \bigcup_{x \in \mathbb{L}} \{F_0 + x, \ldots, F_{255} + x\}$ is formed by all subsets of vertices of C and corresponds to the 26-neighbourhood. The minimal adjacency system $\mathbb{F}_6 = \bigcup_{x \in \mathbb{L}} \mathcal{F}^0(C + x) \cup \mathcal{F}^1(C + x) \cup \mathcal{F}^2(C + x) \cup (C + x)$ generated by the vertices $\mathcal{F}^0(C)$, edges $\mathcal{F}^1(C)$, faces $\mathcal{F}^2(C)$ of C, and C, corresponds to the usually used 6-neighbourhood. The pairs $(\mathbb{F}_{26}, \mathbb{F}_6)$ and $(\mathbb{F}_6, \mathbb{F}_{26})$ are consistent in the following sense: If foreground and background of a binary image are equipped with these adjacency systems, then discrete closed surfaces divide the background into two connected components (Jordan surface theorem) and the Euler numbers of foreground and background can be estimated consistently. If $(\mathbb{F}_{26}, \mathbb{F}_6)$ is used, then foreground and background are treated very unevenly. This is particularly unnatural when foreground and background are just two similar constituents of a micro-structure. To overcome this drawback, Ohser et al. [30] introduced the adjacency systems $\mathbb{F}_{14.1}$ generated by the six congruent tetrahedra F_{139}, F_{141}, F_{163}, F_{177}, F_{197}, and F_{209}, and $\mathbb{F}_{14.2}$ generated by the six tetrahedra F_{43}, F_{141}, F_{149}, F_{169}, F_{177}, and F_{212}. These two adjacency systems are self-consistent, hence foreground and background can be equipped with the same adjacency system without creating paradoxa. The only downside of their use is the loss of symmetry.

3.2 Segmentation

Image segmentation is one of the most important and well-studied areas within image processing, but at the same time, it cannot be considered as solved, and requires specialized solutions most of the time. From a mathematical perspective, image segmentation is an inverse problem, which is frequently ill-posed. There are many reasons for ill-posedness of image segmentation problems, but common causes are insufficient resolution and noise. Both of these causes lead to uncertainty in defining the structures which are to be characterized. Therefore, prior or expert knowledge needs to be incorporated into the design of specialized segmentation routines for most images. Due to this fact, it is beyond the scope of the present paper to give an overview of the segmentation algorithms which have been applied to tomographic images in the past. General overviews of image segmentation algorithms can be found e.g. in [35, 49].

One basic sub-problem of image segmentation is that of image binarization. Loosely speaking, a binarization transforms an arbitrary image into a binary image of the same size. The simplest and most common image binarization procedure is thresholding. It simply decides whether or not a pixel belongs to the foreground independently for each pixel depending on its value (or brightness). Despite its simplicity, this approach remains to be the most generally applicable binarization method, and can lead to good results when combined with adequate noise reduction algorithms. What needs to be answered is the question of how to choose the threshold value. Here, one may differentiate between global and local thresholding algorithms, depending on whether the threshold value is computed for an entire image, or for each pixel, individually.

One example of a widely used rule for computing a threshold value is due to N. Otsu [34]. Under the assumption that the image pixel values' histogram has a bi-modal shape, it searches for the threshold value which separates these two gray value regions best in terms of inner-class gray value variance and intra-class squared distance.

Another segmentation task is the labelling of connected components like grains, pores, or inclusions. While being in principle identical with the same task in two dimensions, labelling becomes much more demanding in 3D. First of all, the discrete connectivity within the lattice has to be defined unambiguously, see Section 3.1 above. Second, keeping track of equivalent labels during the actual labelling is much more complicated, see [29] for more details.

For separation of just touching particles like the grains of a powder or for the reconstruction of cells of an open cell foam, labelling will fail as the objects are connected in the binary image. A combination of the Euclidean distance transform with the watershed transform will however work as long as the objects are "sufficiently spherical" and their sizes do not differ too much: Let $X \subseteq \mathbb{R}^3$ be the set under consideration. The Euclidean distance transform maps each point in $\mathbb{R}^3$ to its shortest distance to the complementary set $\mathbb{R}^3 \setminus X$,

$$\text{EDT} : \mathbb{R}^3 \mapsto [0, \infty) : x \mapsto \min\{||x - y|| : y \in \mathbb{R}^3 \setminus X\}.$$

Clearly, $\text{EDT}(y) = 0$ for all $y \in \mathbb{R}^3 \setminus X$ while ball-shaped regions in X will have local maxima in their centres. On binary images, the EDT can be calculated in linear time. Inversion of the EDT image

$EDT(X \cap \mathbb{L} \cap W)$ turns local maxima into minima: $f(x) = \max\{EDT(X \cap \mathbb{L} \cap W)\} - EDT(x)$. Now the watershed transform assigns a connected region to each local minimum. The transform can be interpreted as the flooding of the topographic surface $\{(x, f(x)) : x \in \mathbb{L} \cap W\}$: Water rises uniformly with growing grey value from all local minima. Watersheds are formed by all pixels where waters from different sources meet. This idea was turned into an efficient algorithm by Vincent and Soille [47]. Finally, the image is segmented into regions and the system of watersheds dividing them. In order to use the sketched separation strategy successfully, superfluous local minima caused by discretisation effects, shape distortions, and binarisation errors, have to be suppressed. Alterating the watershed transform such that regions smaller than a pre-defined volume are united with larger regions [46] or smoothing the EDT image using the morphological h-minima transform [42, Chapter 6] are well-tested methods for this. The latter even allows to cope with large size differences when the parameter h is adapted to total grey value [15], [33, Section 4.2.6].

4   Quantitative Analysis: Use cases

In applications, the micro-structures under investigation are typically not deterministic but show a certain degree of randomness. Therefore, the content of an image may be interpreted as a random set. A wide range of geometric characteristics for such random sets has been established [45]. Quantitative image analysis provides the methods to measure these characteristics from image data [33]. In practice, suitable characteristics as well as the methods to determine them are chosen depending on the type of micro-structure: its invariance properties, the number of components it consists of and whether it has a natural object structure or not.

A typical assumption is that the material under investigation is a macroscopically homogeneous and isotropic random set. Macroscopically homogeneous roughly means that the random structure observed in the sample does on average not depend on the position of the sample within the specimen. Isotropic are structures which are - again on average - invariant with respect to rotations of the sample, too.

In this section we will discuss several analysis techniques by the example of typical use cases.

4.1   Open cell foam

An open cell foam is formed by a connected system of struts which are given by the edges of approximately polyhedral cells. A typical analysis task for such a material is to analyse the distributions of the cells' size and shape. This information can be derived from the intrinsic volumes (also Minkowski functionals or quermass integrals) – the volume V, the surface area S, the integral of mean curvature M and the Euler number χ. For a convex object, M is up to a constant the mean width. The Euler number is a topological characteristic alternately counting the connected components, the tunnels, and the holes of the particle. For a convex body, we have $\chi = 1$, for a torus $\chi = 1 - 1 = 0$, and for a sphere $\chi = 1 + 1 = 2$. Efficient algorithms for the simultaneous measurement of all intrinsic volumes from 3D image data are available [33, Chapter 5].

Useful further characteristics like the isoperimetric shape factors $f_1 = 6\sqrt{\pi}V/\sqrt{S^3}, f_2 = 48\pi^2 V/M^3$, $f_3 = 4\pi S/M^2$ can be derived from the intrinsic volumes. These shape factors are normalized such that $f_1 = f_2 = f_3 = 1$ for a ball. Deviations from 1 thus describe various aspects of deviations from ball shape. Other shape characteristics are e. g. the ratio of the volumes of an object and its convex hull characterising the convexity of the object or the ratios of the edge lengths of the minimal-volume bounding cuboid characterising the elongation of the object.

In order to measure geometric cell characteristics the pore space has to be divided into single cells using the cell reconstruction method described in Section 3.2 above. An application of this method to an open copper foam is shown in Figure 2. The same techniques may also be used to separate the cells in closed cell foams as well as the particles in granular materials. For particles such as fibers which have a highly non-spherical shape the method will fail.
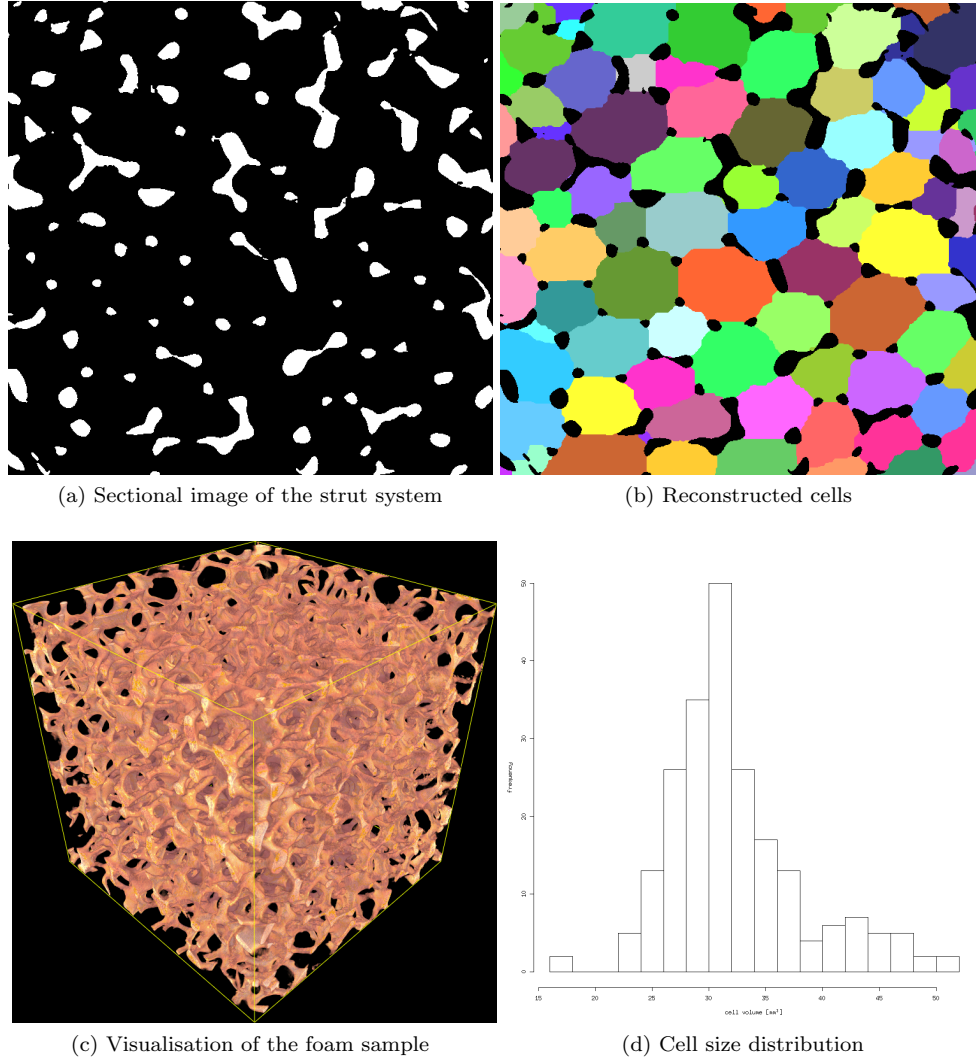
(a) Sectional image of the strut system

(b) Reconstructed cells

(c) Visualisation of the foam sample

(d) Cell size distribution

Figure 2: Analysis of an open cell copper foam using cell reconstruction. Sample: Duocell foam. Imaging: Fraunhofer ITWM. Pixel size $38.15\,\mu$m, sample size approximately $24.0 \times 24.6 \times 24.4\,\mathrm{mm}^3$.

4.2 Greenland firn (sintered snow)

For components of macroscopically homogeneous micro-structures without a natural object structure, we use the densities of the intrinsic volumes as basic geometric characteristics. Instead of the absolute values of the four functionals, now their ratio to the sample volume is considered which yields the volume fraction V_V, the specific surface area S_V, and the densities of the integral of mean curvature M_V and the Euler number χ_V. For porous media, the porosity is defined as $1 - V_V$. A shape factor - the structure model index (SMI) - can be derived via $f_{\mathrm{SMI}} = 4\pi V_V M_V / S_V^2$ [32]. It takes values 4, 3, and 0 for ideal systems of non-overlapping balls, cylinders, and planes, respectively.

As an example we analysed firn samples from the firn core B26 which was drilled during the North Greenland traverse of the Alfred Wegener Institute Bremerhaven in 1995 [14]. Five firn samples taken from different depths within the ice core were imaged using a portable μCT scanner inside a cold room at $-25°$C. From the resulting grey value images, binary images of the pore system of the firn were obtained by global thresholding. Visualisations of the firn samples are shown in Fig. 3.

The estimated values for the intrinsic volume densities and the SMI are given in Table 1. They show an increase of f_{SMI} with increasing depth. The starting value around 3 indicates a cylindrical structure. The visualisations of the deeper samples already show a number of isolated spherical pores. Therefore, a further increase of f_{SMI} towards 4 can be expected when going deeper within the firn core.

depth [m]	porosity [%]	$S_V[m^{-1}]$	$M_V[m^{-2}]$	$\chi_V[m^{-3}]$	f_{SMI}
56	15.71	1070.36	1.80e6	-1.21e8	2.954
60	13.16	890.00	1.57e6	-2.56e7	3.135
69	10.11	755.71	1.61e6	8.93e7	3.373
72	9.06	697.19	1.52e6	1.03e8	3.410
74	7.83	644.49	1.55e6	1.46e8	3.503

Table 1: Intrinsic volume densities and SMI for firn samples with different porosities.

4.3 Glass fibre reinforced polymers

With increasing resolutions and sample sizes, the number of samples for which macroscopic homogeneity cannot be assumed rises, too. Global quantitative analysis as shown in the previous sections 4.1 and 4.2 yields only limited information in these cases. Thus additional local analysis is needed. This can be achieved by tessellating the sample by sub-volumes, sliding a sub-volume through the sample or assigning local measurement values to each pixel. Hilfer [20] defines local porosity in each pixel as the porosity in a cubic sub-volume centered at this pixel. This idea can of course be generalized to all densities of the intrinsic volumes as defined in Section 4.2. In this section, we present a local analysis method for fibre systems combining the locality of measurements in each pixel with the robustness of averaging over subvolumes.

Fibre systems like the fibre component in fibre reinforced composites, non-wovens, or fibre-reinforced concretes can be mathematically modelled as an anisotropic randomly oriented fibre system Ξ in 3D Euclidean space $\mathbb{R}^3$. The directional distribution of the fibres is crucial for materials properties like the mechanical strength of fibre reinforced composites or the filtration efficiency of a non-woven. Based on 3D image data, we want to estimate the direction distribution $R(A) = 1/(2\pi V(W))\mathbb{E}\int_{W \cap \Xi} \mathbb{I}_A(\nu(x))dx$, where $A \subseteq \mathbb{S}_+^2$ is a measurable set of non-oriented directions, $\nu(x)$ is the direction of the fibre in point x. The expectation $\mathbb{E}$ is taken with respect to the random fibre system Ξ.

We estimate the directional distribution R by calculating the local fibre direction in each pixel. Recently, several approaches to local direction estimation without segmentation of individual fibres have been developed [1, 27, 51]. Here we use the method based on the Hessian matrix of second order partial derivvatives of the grey values, that has proved to be fast and robust in many applications.

Let g_σ be an isotropic Gaussian smoothing kernel in $\mathbb{R}^3$ with parameter $\sigma > 0$ adjusted to the fibre radius, $\sigma \approx r$. Now consider the Hessian matrix $H(x)$ of second derivatives of the image f smoothed by

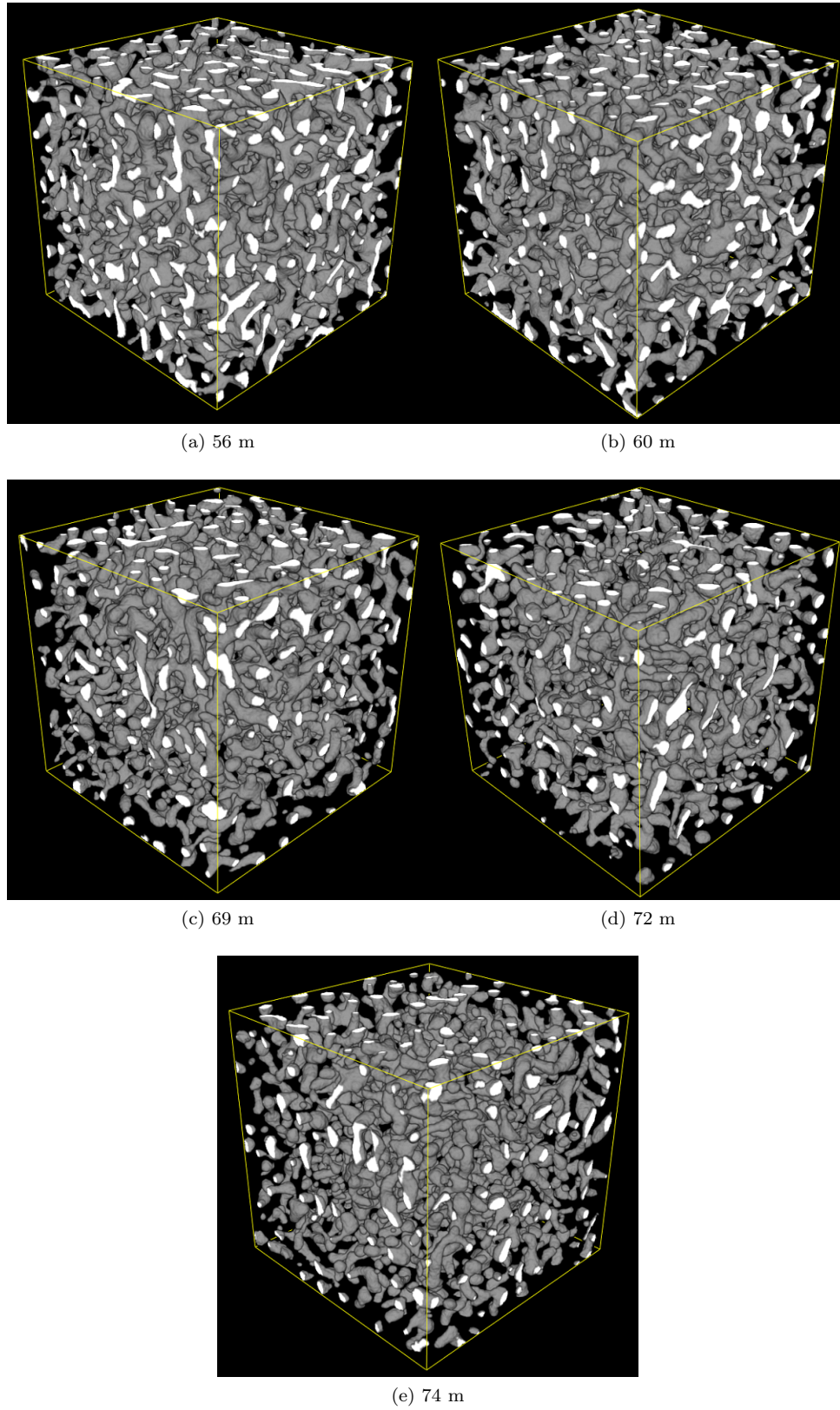(a) 56 m

(b) 60 m

(c) 69 m

(d) 72 m

(e) 74 m

Figure 3: Visualisations of reconstructed tomographic images of firn samples from five different depths. Samples and imaging: J. Freitag, Alfred-Wegener Institute for Polar and Marine Research, Bremerhaven. Pixel size $40\,\mu$m, sample size approximately $(16\,\mathrm{mm})^3$. The pore system is visualised.

g_σ:

$$H(x) = \left(\frac{\partial^2}{\partial x_i \partial x_j} \right) (f * g_\sigma)(x), \qquad x \in \mathbb{R}^3.$$

The eigenvectors of H carry information about directions of the random field Ξ at x. For a fibrous structure, the least gray value variation is expected along the fibre. Thus the eigenvector corresponding to the smallest eigenvalue of the Hessian matrix $H(x)$ at x is interpreted as the local direction $\nu(x)$. Cumulation of these local direction estimates yields the volume weighted direction distribution R as defined above.

The outer product of the components ν_1, ν_2, ν_3 averaged with respect to R yields the so-called second order orientation tensor $\langle a_{ij} \rangle$. That is:

$$a_{ij} = \int \nu_i \nu_j \, R(d\nu), \quad i,j = 1, 2, 3.$$

An estimator for the components a_{ij} is obtained by averaging the components of the local direction $\nu(x)$ over small subvolumes W:

$$\widehat{a}_{ij} = \sum_{x \in W \cap \mathbb{L} \cap \Xi} \nu_i(x)\nu_j(x). \tag{1}$$

The orientation tensors are widely used in simulation of materials properties in order to incorporate anisotropic local behaviour.

A typical example of a glass fibre composite is the sample shown in Figure 4. The thickness of the fibres is constant, approximately $10\,\mu$m. The fibre weight fraction of 60% yields an approximate fibre volume fraction of 50%. While the contrast between fibre and matrix component is good, this high fibre volume fraction prevents segmentation of individual fibres. Moreover, the high density of the sample caused a decline of the grey values towards the centre of the image. Consequently, global thresholding would erroneously imply that the local fiber volume fraction varies strongly. A remedy is a global grey value correction, known as shading correction from 2D image analysis: The morphologically opened image is pixel-wise subtracted from the original. In this image, the local fibre directions can be estimated and the results are in good agreement with both visual impression and theoretical expectations: Due to the injection molding the fibres are oriented in fill direction near the sample boundaries while lying perpendicular to this direction in the core of the sample.

A second example is the glass fibre composite shown in Figure 1. As the previous example, the sample is not homogeneous as subvolumes close to the welding seam behave differently from subvolumes further away from it. We analyse the two subvolumes visualised in Figure 1 using the Hessian matrix as described above and estimate the orientation tensor a_{ij} via (1), averaging over the complete subvolumes. Denote by $\lambda_1 \geq \lambda_2 \geq \lambda_3 \geq 0$ the eigenvalues of the orientation tensor in descending order. Fisher et al. [13] use descriptors derived from these eigenvalues to classify girdle and clustered distributions on the sphere: The shape $\gamma = \log(\lambda_1/\lambda_2)/\log(\lambda_2/\lambda_3)$ and the strength $\xi = \log(\lambda_1/\lambda_3)$. A value of γ below 1 indicates a girdle shape while $\gamma > 1$ is typical for clustered shapes. If the value of ξ is however close to 0, than the directional distribution is isotropic or in some other way neither clustered nor girdle-like. For the subvolume close to the weldings seam we get $\gamma = 0.28, \xi = 1.65$ while $\gamma = 0.63, \xi = 1.98$ away from the welding seam. Thus both distributions are girdle like. However, the latter is more concentrated, tending towards a clustered one.

4.4 Fibre felt

Another example for a fibre structure is a polymer felt used for dewatering paper pulp, imaged using holotomography [10], see Figure 4.4. This microstructure is formed by two fibre fractions - thick and thin ones. The different fibre thicknesses can be quantified using the spherical granulometry. This transform assigns to each pixel the size of the largest ball inscribed in the structure and covering it. More precisely, let Ξ denote a random closed set, B_r the ball of radius r and $\Xi \circ B_r$ the morphological opening of Ξ with B_r. The granulometry distribution function
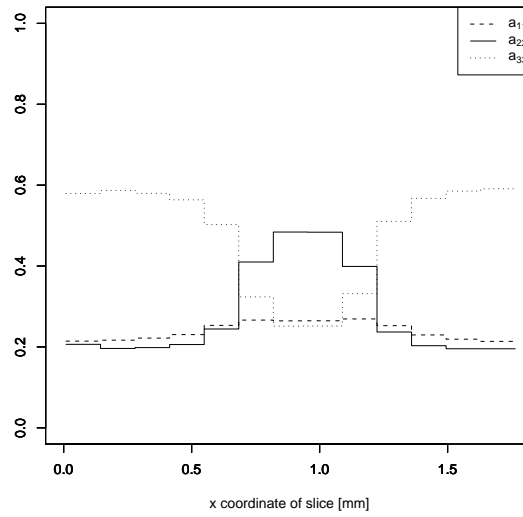
$$G(d) = 1 - \frac{1 - V_V(\Xi \circ B_{d/2})}{1 - V_V(\Xi)}, \qquad d \geq 0$$
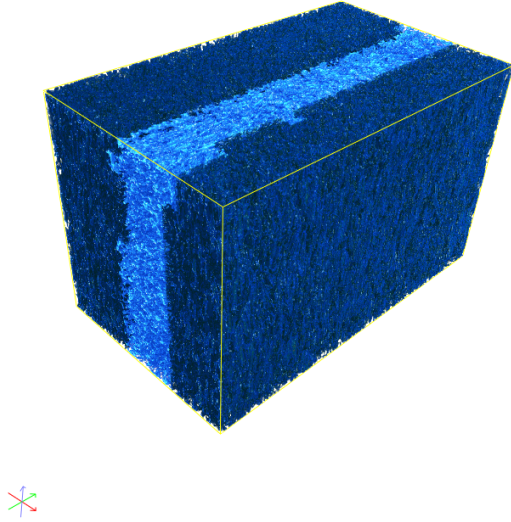
(a) Volume rendering
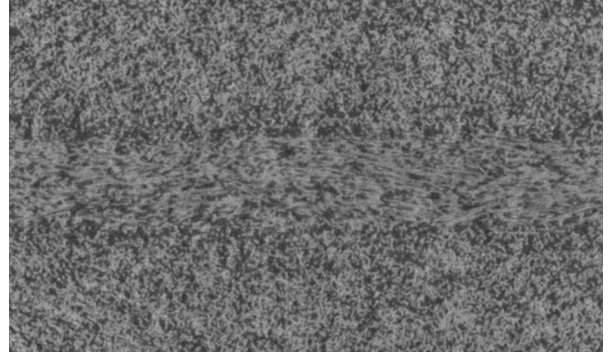
(b) Slice through shading corrected image

(c) Diagonal elements of the orientation tensor, averaged over
thick slices orthogonal to the x-axis

Figure 4: Glass fibre reinforced polymer. Sample and imaging: Institut für Verbundwerkstoffe Kaiserslautern. Fibre width approximately $10 \, \mu$m, pixel size $3 \, \mu$m, sample size approximately $1.8 \times 3 \times 3 \, \text{mm}^3$.

yields a volume weighted generalized size distribution. It can be estimated from the binary image $\Xi \cap \mathbb{L} \cap W$ by successive morphological openings with growing balls $\Xi \cap \mathbb{L} \cap W \circ B_{r_i}$ until all foreground pixel have disappeared. Finally each pixel x is assigned the diameter of the ball used as structuring element in the step where x disappeared for the first time. The resulting image is called ultimate opening [4].

A much more efficient algorithm is based on the medial axis $M(\Xi \cap \mathbb{L} \cap W)$, which is the set of all centers of maximal inscribed balls. Observe that the original structure can be reconstructed using the values of the Euclidean distance transform $\text{EDT}(\Xi \cap \mathbb{L} \cap W)$ at the pixels forming the medial axis. Sort these values in increasing order and respecting this order draw balls with radius $\text{EDT}(x)$ at all $x \in M(\Xi \cap \mathbb{L} \cap W)$, such that larger values overwrite smaller ones. Pixel-wise multiplication by 2 then yields the ultimate opening.

For the fibre felt, the granulometry distribution can be interpreted as the volume weighted thickness distribution. The histogram in Figure 4.4 features two clear modes corresponding to the thin and thick fibres forming the felt micro-structure. A minus-sampling edge correction was applied to remove too low thickness values at the image borders. That is, only the thickness values of pixels 40 pixels away from the image borders are taken into account. A morphological opening with a ball, whose diameter is larger than the thickness of the thin fibres, yields the system of the thick fibres. A white-top-hat transform (subtract opening result from original image) then yields the thin ones. The local fibre directions can be estimated as described in Section 4.3 using the estimated thickness values for the thin and the thick fibres, respectively. Masking with the separated images, yields the directional distributions for the thin and the thick fibres. The eigenvalue analysis of the orientation tensor yields $\gamma_{\text{thin}} = 1.43, \xi_{\text{thin}} = 0.04$ and $\gamma_{\text{thick}} = 2.43, \xi_{\text{thick}} = 0.88$. Thus the direction distribution of the thin fibres is neither clustered nor girdle-like while the direction distribution of the thick fibres tends to be clustered.

4.5   Early stage closed cell foam

One way of producing metal foams is the so called powder foaming method where both the bulk material and the foaming agent in powder form are mixed, pressed, and subsequently heated. Here, we consider aluminium foams with titanium hydride TiH_2, which when heated, releases hydrogen that in turn blows up the mixture. In order to improve the foaming process and to tightly control the resulting pore size distribution, a deep understanding of the pore generation is needed.

To this end, aluminium foam samples stopped during early pore formation were imaged by synchrotron μCT [17, 19]. In the resulting images, the three components - metal matrix, foaming agent, and pores, are clearly visible due to their well separated grey values. Thus, after a median filter for noise removal, global thresholding yields the titanium hydride and the pores, respectively. An additional preprocessing step is necessary to avoid the physically impossible "particles" within the pores, not connected to the matrix: Labelling of the background, subsequent extraction of the largest component, and finally inverting the binary image, is equivalent to filling the small holes, in the present case. As a side effect, there is a small number of pixels assigned to the TiH_2 as well as to the pore space. These are removed from the pore space by a pixel-wise subtraction.

Now, given binary images of the foaming agent and the pore system, we can tackle the actual analysis question, whether the pores develop in the vicinity of the foaming agent particles or whether some other effect dominates the early pore generation.

Let Ξ and Ψ denote the random closed sets of the pores and the TiH_2, respectively. They can be assumed to be macroscopically homogeneous. Naively, one would check whether Ξ and Ψ correlate by checking whether
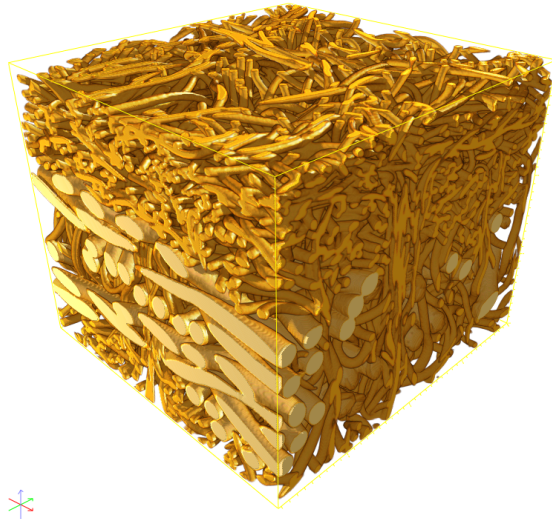
$$\mathbb{P}(x \in \Xi, y \in \Psi) = \mathbb{P}(x \in \Xi)\mathbb{P}(y \in \Psi) \quad \text{for all} \quad x, y \in \mathbb{R}^3.$$

However, leftovers of the TiH_2 can be observed within the bulk only. That is, we observe $\Psi' = \Psi \cap \overline{\Xi^c}$, where $\overline{\Xi^c}$ denotes the closure of the complement of the pore system Ξ. Consequently, the pore system Ξ and the observed TiH_2 leftovers Ψ' will be correlated in any case.
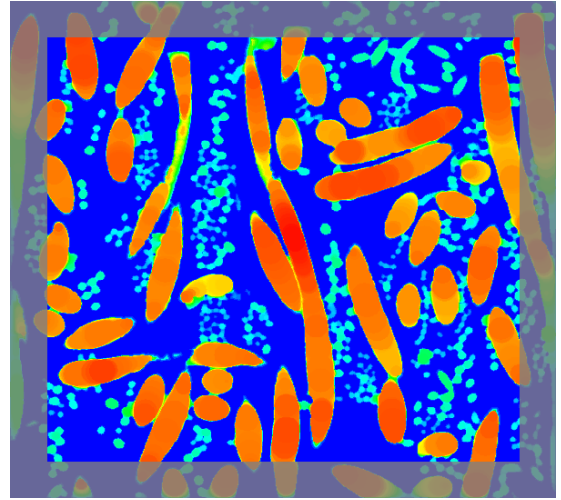
If Ξ and Ψ are independent we have however

$$\begin{aligned}\mathbb{P}(x \in \Xi, y \in \Psi') &= \mathbb{P}(x \in \Xi, y \in \overline{\Xi^c}, y \in \Psi) \\ &= \mathbb{P}(x \in \Xi, y \in \overline{\Xi^c})\mathbb{P}(y \in \Psi) \quad \text{for all} \quad x, y \in \mathbb{R}^3.\end{aligned} \quad (2)$$
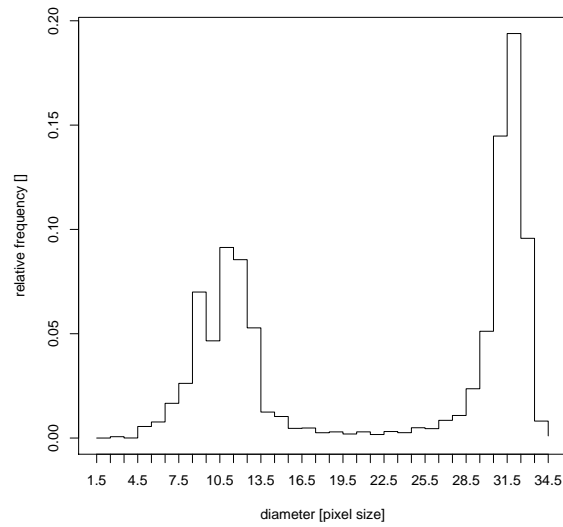
(a) Volume rendering

(b) Slice through colour coded granulometry image

(c) Histogram of spherical granulometry distribution

Figure 5: Fibre felt, imaged by L. Helfen at ESRF using holotomography [10]. Pixel size $6.65\,\mu$m, sample size approximately $(3.4\,\mathrm{mm})^3$. The shaded region in the slice (b) indicates the edge correction.

Deviation from this necessary condition would thus indicate correlation. In order to check it based on image data, first observe that $\mathbb{P}(x \in \Xi, y \in \Psi) - \mathbb{P}(x \in \Xi)\mathbb{P}(y \in \Psi) = \mathbb{P}(x \in \Xi, y \in \Psi) - V_V(\Xi)V_V(\Psi) = \text{cov}_{\Xi,\Psi}(x,y)$ is the cross-covariance function of the sets Ξ and Ψ. Due to the macroscopic homogeneity, it depends on the difference $h = x - y$ only:

$$\text{cov}_{\Xi,\Psi}(h) = \mathbb{P}(x \in \Xi, x + h \in \Psi) - V_V(\Xi)V_V(\Psi), \quad h \in \mathbb{R}^3.$$

We can now write the necessary condition (2) in terms of the cross-covariance function as $\text{cov}_{\Xi,\Psi'}(h) = \text{cov}_{\Xi,\overline{\Xi^c}}(h)V_V(\Psi)$. We note that $V_V(\Psi) = V_V(\Psi')/(1 - V_V(\Xi))$ and deduce the characteristic

$$t(h) = \frac{\text{cov}_{\Xi,\Psi'}(h)(1 - V_V(\Xi))}{\text{cov}_{\Xi,\overline{\Xi^c}}(h)V_V(\Psi')},$$

which can be estimated efficiently from the respective binary images exploiting the discrete Fourier transform [25, 38]. The relationship $t \equiv 1$ is a necessary criterion for the sets Ξ and Ψ to be independent. Figure 6 shows visualizations of foam samples produced using the two different precursor materials AW-6061 and AlSi7. For AW-6061, the strong deviation of t from 1 indicates short-range correlation of pores and foaming agent. For the AlSi7 samples, the pore initiation by the silica inclusions dominates, thus there is no strong correlation between pores and TiH^2. See [17] for details. Distance values up to $\sqrt[3]{0.7}\,\mu\text{m}$ are excluded from the analysis since pixels at the interfaces between the three constituents cannot be assigned reliably due to the so-called halo or partial volume effect: The grey values in these pixels are a weighted mean of the grey values of the two neighbouring constituents. If the restricting resource for the computation is memory instead of time, an alternative rationale can be used: If pore space and foaming agent were independent, then the observable volume fraction of TiH_2 should be constant, no matter at which distance from the pore system. This leads to the necessary condition that the fraction of TiH_2 observed in the intersection of the bulk with stepwise dilations of the pore system $\Xi \oplus B_r$ should be constant. Fast stepwise dilations by balls with growing radius can be achieved by simple global thresholding of the Euclidean distance transform performed on Ξ^c. For details on this method see [38] or [33, Section 5.5.2].

5   Conclusion

Computed tomography combined with quantitative image analysis offer a wide variety of new possibilities to characterise micro-structures. Neither the use cases chosen for this paper nor the analysis methods presented cover the complete range. They do however represent classes of structures – porous media and (fibre) composites – for which 3D imaging and image analysis are particularly useful and sought-after. The methods are restricted to well-tested, general ones being applicable in various applications. Nevertheless, the selection remains subjective and incomplete. Missing are for instance, non-additive functionals, see e. g. [29] for a definition of a mean diameter of percolating pores, further particle characteristics.

Geometric characterisation opens the door to reconstruction of micro-structures or so-called virtual materials design. Starting from the characteristics measured in the 3D image, a stochastic geometric model is fitted to the micro-structure. Numerical simulation of properties like thermal conductivity, elasticity, or filtration efficiency at the micro-scale ad homogenisation yield macroscopic materials properties. Selective alternation of the model parameters and therewith of the micro-structure allows to study the effect on the physical property by simulating in realisations of the new micro-structure. This yields a deeper understanding of the relation between micro-structure and materials properties and even enables optimisation of the micro-structure with respect to the desired materials property. Frequently used models are random systems of cylinders for fibers, random dense packings for granular media, and random Laguerre tessellations for foams, see [22] for an overview and [2, 36, 40, 41] for examples.

Correspondence address:
Dr. Claudia Redenbach

(a) AlSi7

(b) AW-6061
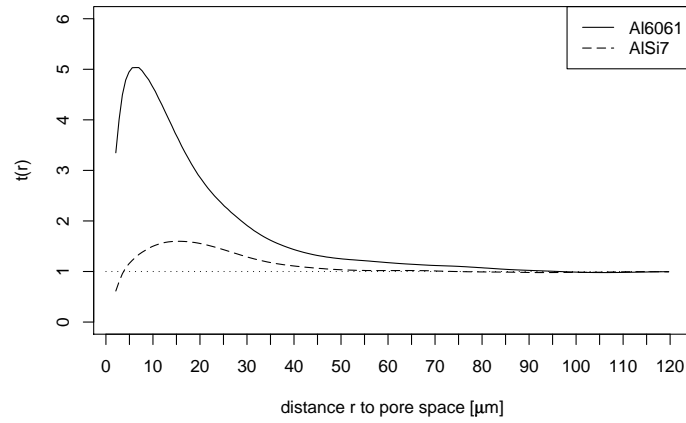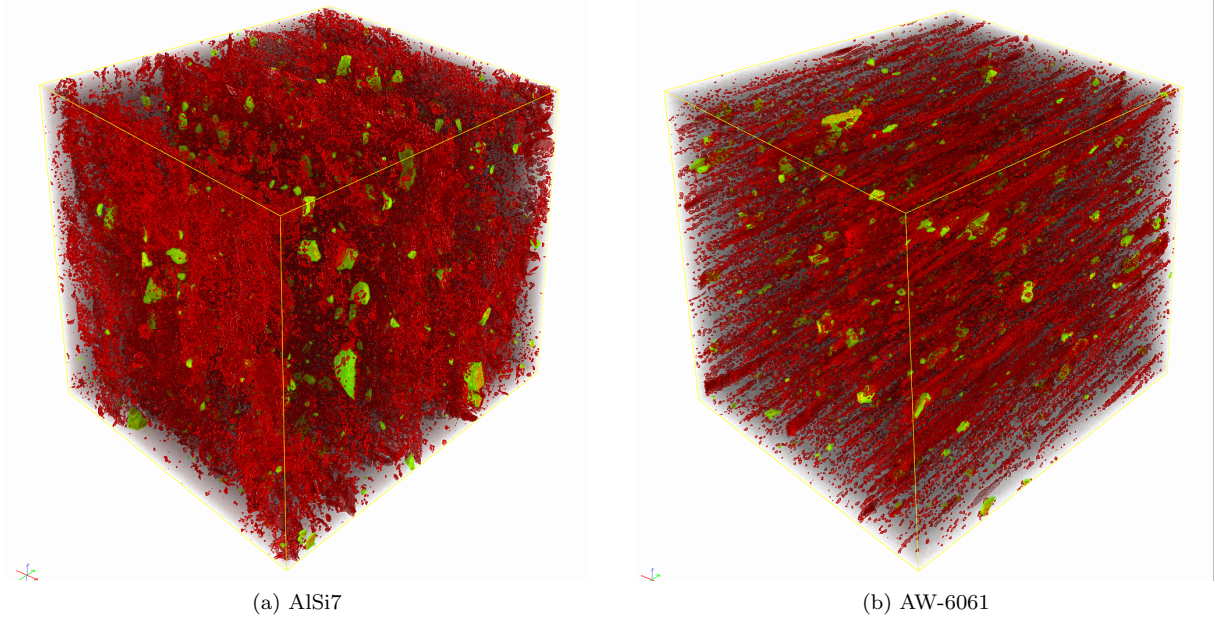

(c) Cross correlation

Figure 6: Volume renderings of the AW-6061 and AlSi7 foam samples, red - pore space, green - foaming agent leftovers. Images taken by L. Helfen at ESRF, pixel size $0.7\,\mu$m, sample size $(4.62\,\text{mm})^3$.

University of Kaiserslautern, Mathematics Department, Erwin-Schrödinger Straße, D-67663 Kaiserslautern
Tel.: +49-(0)631-205-3620
Fax: +49-(0)631-205-2748
e-mail: redenbach@mathematik.uni-kl.de

List of figure and table captions.

References

[1] H. Altendorf and D. Jeulin. 3d directional mathematical morphology for analysis of fiber orientations. *Image Analysis and Stereology*, 28(3):143–153, 2009.

[2] H. Altendorf and D. Jeulin. Modeling fiber systems using random walks. In *3rd International Workshop: 3D Imaging, Analysis, Modeling and Simulation of Macroscopic Properties*, Fontainebleau, April 2010.

[3] J. Banhart, editor. *Advanced Tomographic Methods in Materials Research and Engineering*. Oxford University Press, 2008.

[4] S. Beucher. Numerical residues. *Image Vision Comput*, 25:405–415, 2007.

[5] D. Blavette, A. Bostel, J. M. Sarrau, B. Deconihout, and A. Menand. An atom probe for three-dimensional tomography. *Nature*, 363:432–435, 1993.

[6] P. Bleuet, P. Cloetens, P. Gergaud, D. Mariolle, N. Chevalier, R. Tucoulou, J. Susini, and A. Chabli. A hard x-ray nanoprobe for scanning and projection nanotomography. *Rev. Sci. Instrum.*, 80(5):056101, 2009.

[7] R. A. Brooks and G. DiChiro. Statistical limitations in x-ray reconstructive tomography. *Med. Phys.*, 3:237–240, 1976.

[8] D. Chapman, W. Thomlinson, R. E. Johnston, D. Washburn, E. Pisano, N. Gmür, Z. Zhong, R. Menk, F. Arfelli, and D. Sayers. Diffraction enhanced x-ray imaging. *Phys. Med. Biol.*, 42(11):2015, 1997.

[9] P. Cloetens, W. Ludwig, J. Baruchel, D. V. Dyck, J. Landuyt, J. P. Guigay, and M. Schlenker. Holotomography: Quantitative phase tomography with micrometer resolution using hard synchrotron radiation x-rays. *Appl. Phys. Lett.*, 75:2912–2914, 1999.

[10] P. Cloetens, W. Ludwig, E. Boller, L. Helfen, L. Salvo, R. Mache, and M. Schlenker. Quantitative phase contrast tomography using coherent synchrotron radiation. *Proc. SPIE*, 4503(1):82–91, 2002.

[11] M. Dierolf, A. Menzel, P. Thibault, P. Schneider, C. M. Kewish, R. Wepf, O. Bunk, and F. Pfeiffer. Ptychographic x-ray computed tomography at the nanoscale. *Nature*, 467:436–439, 2010.

[12] M. Feser, J. Gelb, H. Chang, H. Cui, F. Duewer, S. H. Lau, A. Tkachuk, and W. Yun. Sub-micron resolution ct for failure analysis and process development. *Meas. Sci. Tech.*, 19(9):094001, 2008.

[13] N. Fisher, T. Lewis, and B. Embleton. *Statistical analysis of spherical data*. Cambridge University Press, Cambridge, 1987.

[14] J. Freitag, F. Wilhelms, and S. Kipfstuhl. Microstructure-dependent densification of polar firn derived from x-ray microtomography. *Journal of Glaciology*, 50(169):243–250, 2004.

[15] M. Godehardt and K. Schladitz. Geometric characterisation of light weight composites using computer tomographic images. In *Proceedings of the 9th European NDT Conference*, Berlin, 2006.

[16] G. Harding and J. Kosanetzky. Scattered x-ray beam nondestructive testing. *Nucl. Instr. & Meth. in Phys. Res. A*, 280(2–3):517–528, 1989.

[17] L. Helfen, T. Baumbach, P. Cloetens, H. Stanzick, K. Schladitz, and J. Banhart. Investigation of the pore initiation process in metal foams by synchrotron-radiation computed tomography. *Appl. Phys. Lett.*, 86:231907, 2005.

[18] L. Helfen, A. Myagotin, A. Rack, P. Pernot, P. Mikulík, M. Di Michiel, and T. Baumbach. Synchrotron-radiation computed laminography for high-resolution three-dimensional imaging of flat devices. *phys. status. solidi A*, 204(8):2760–2765, 2007.

[19] L. Helfen, H. Stanzick, J. Ohser, K. Schladitz, P. Rejmánková-Pernot, J. Banhart, and T. Baumbach. Investigation of the foaming process of metals by synchrotron-radiation imaging. In B. M. Norbert Meyendorf, George Y. Baaklini, editor, *Proceedings SPIE 5045: Testing, Reliability, and Application of Micro- and Nano-Material Systems*, volume 5045, pages 254–265, 2003.

[20] R. Hilfer. Local porosity theory and stochastic reconstruction. In K. R. Mecke and D. Stoyan, editors, *Statistical Physics and Spatial Statistics*, volume 554 of *LNP*, pages 203–241. Springer, Heidelberg, 2000.

[21] J. Hsieh. *Computed Tomography: Principles, Design, Artifacts and Recent Advances*. SPIE Press, Bellingham, WA, 2nd edition, 2009.

[22] D. Jeulin. Random structures in physics. In M. Bilodeau, F. Meyer, and M. Schmitt, editors, *Space, Structure and Randomness*, volume 183 of *Lecture Notes in Statistics*, pages 183–222. Springer, New York, 2005. Contributions in Honor of Georges Matheron in the Fields of Geostatistics, Random Sets, and Mathematical Morphology.

[23] A. C. Kak and M. Slaney. *Principles of Computerized Tomographic Imaging*. IEEE Press, New York, 1988.

[24] A. King, G. Johnson, D. Engelberg, W. Ludwig, and J. Marrow. Observations of intergranular stress corrosion cracking in a grain-mapped polycrystal. *Science*, 321(5887):382–385, 2008.

[25] K. Koch, J. Ohser, and K. Schladitz. Spectral theory for random closed sets and estimating the covariance via frequency space. *Adv. Appl. Prob.*, 35:603–613, 2003.

[26] A. M. Korsunsky, N. Baimpas, X. Song, J. Belnoue, F. Hofmann, B. Abbey, M. Xie, J. Andrieux, T. Buslaps, and T. K. Neo. Strain tomography of polycrystalline zirconia dental prostheses by synchrotron x-ray diffraction. *Acta Mater.*, 59(6):2501–2513, 2011.

[27] M. Krause, J. Hausherr, B. Burgeth, C. Herrmann, and W. Krenkel. Determination of the fibre orientation in composites using the structure tensor and local x-ray transform. *J. Material Science*, 45(4):888–896, Feb 2010.

[28] A. Kubis, G. Shiflet, R. Hull, and D. Dunn. Focused ion-beam tomography. *Metallurg. & Mater. Trans. A*, 35:1935–1943, 2004.

[29] J. Ohser, C. Ferrero, O. Wirjadi, A. Kuznetsova, J. Dll, and A. Rack. Estimation of the probability of finite percolation in porous microstructures from tomographic images. *Int J Mater Res*, (this issue), 2012.

[30] J. Ohser, W. Nagel, and K. Schladitz. The Euler number of discretized sets – on the choice of adjacency in homogeneous lattices. In K. R. Mecke and D. Stoyan, editors, *Morphology of Condensed Matter*, volume 600 of *LNP*, pages 275–298, Berlin, 2002. Springer.

[31] J. Ohser, W. Nagel, and K. Schladitz. Miles formulae for Boolean models observed on lattices. *Image Anal. Stereol.*, 28(2):77–92, 2009.

[32] J. Ohser, C. Redenbach, and K. Schladitz. Mesh free estimation of the structure model index. *Image Anal. Stereol.*, 28:101–107, 2009.

[33] J. Ohser and K. Schladitz. *3d Images of Materials Structures – Processing and Analysis*. Wiley VCH, Weinheim, 2009.

[34] N. Otsu. A threshold selection method from gray level histograms. *IEEE Trans. Systems, Man and Cybernetics*, 9:62–66, Mar. 1979.

[35] N. Pal and S. Pal. A review on image segmentation techniques. *Pattern Recognition*, 26(9):1277 – 1294, 1993.

[36] C. Peyrega, D. Jeulin, C. Delisée, and J. Malvestio. 3d morphological modelling of a random fibrous network. *Image Anal. Stereol.*, 28:129–141, 2009.

[37] A. Rack, F. García-Moreno, C. Schmitt, O. Betz, A. Cecilia, A. Ershov, T. Rack, J. Banhart, and S. Zabler. On the possibilities of hard x-ray imaging with high spatio-temporal resolution using polychromatic synchrotron radiation. *J. X-Ray Sci. Tech.*, 18:429–441, 2010.

[38] A. Rack, L. Helfen, T. Baumbach, S. Kirste, J. Banhart, K. Schladitz, and J. Ohser. Analysis of spatial cross-correlations in multi-constituent volume data. *Journal of Microscopy*, 232(2):282–292, 2008.

[39] A. Rack, S. Zabler, B. R. Müller, H. Riesemeier, G. Weidemann, A. Lange, J. Goebbels, M. Hentschel, and W. Görner. High resolution synchrotron-based radiography and tomography using hard x-rays at the bamline (bessy ii). *Nucl. Instr. & Meth. in Phys. Res. A*, 586(2):327–344, 2008.

[40] C. Redenbach. Modelling foam structures using random tessellations. In V. C. et al., editor, *Stereology and Image Analysis. Ecs10: Proceeding of the 10th European Conference of ISS.*, volume 4 of *The MIRIAM Project Series*, Bologna, 2009. ESCULAPIO Pub. Co.

[41] K. Schladitz, S. Peters, D. Reinel-Bitzer, A. Wiegmann, and J. Ohser. Design of acoustic trim based on geometric modeling and flow simulation for non-woven. *Computational Materials Science*, 38:56–66, 2006.

[42] P. Soille. *Morphological image analysis*. Springer Verlag, 1999.

[43] S. R. Stock. *MicroComputed Tomography: Methodology and Applications*. CRC Press, Boca Raton, 2008.

[44] S. R. Stock, F. De Carlo, and J. D. Almer. High energy x-ray scattering tomography applied to bone. *J. Struct. Biol.*, 161(2):144–150, 2008.

[45] D. Stoyan, W. S. Kendall, and J. Mecke. *Stochastic Geometry and Its Applications*. Wiley, Chichester, 2nd edition, 1995.

[46] F. B. Tek, A. G. Dempster, and I. Kale. Blood cell segmentation using minimum area watershed and circle Radon transformations. In C. Ronse, L. Najman, and E. Decencire, editors, *Proc. Int. Symp. on Mathematical Morphology*, volume 30 of *Computational Imaging and Vision*, pages 441–454, Dordrecht, April 2005. Springer.

[47] L. Vincent and P. Soille. Watersheds in digital spaces: An efficient algorithm based on immersion simulation. *IEEE Transactions on Pattern Analysis and Machine Intelligence*, 13(6):583–598, 1991.

[48] T. Weitkamp, A. Diaz, C. David, F. Pfeiffer, M. Stampanoni, P. Cloetens, and E. Ziegler. X-ray phase imaging with a grating interferometer. *Opt. Express*, 13(16):6296–6304, Aug 2005.

[49] O. Wirjadi. Survey of 3d image segmentation methods. Technical Report 123, Fraunhofer ITWM, Kaiserslautern, 2007.

[50] O. Wirjadi. *Models and Algorithms for Image-Based Analysis of Microstructures*. PhD thesis, Technical University Kaiserslautern, 2009.

[51] O. Wirjadi. *Models and Algorithms for Image-Based Analysis of Microstructures*. PhD thesis, Technische Universität Kaiserslautern, 2009.

[52] N. Zoeger, C. Streli, P. Wobrauscheck, C. Jokubonis, G. Pepponi, P. Roschger, J. Hofstaetter, A. Berzelanovich, D. Wegrzynek, E. Chinea-Cano, A. Markowicz, R. Simon, and G. Falkenberg. Determination of the elemental distribution in human joint bones by sr micro xrf. *X-Ray Spectrom.*, 37(1):3–11, 2008.